IEEE Access
Multidisciplinary | Rapid Review | Open Access Journal

Received June 3, 2021, accepted June 15, 2021, date of publication June 22, 2021, date of current version July 1, 2021.

Digital Object Identifier 10.1109/ACCESS.2021.3091578

Histological Image Segmentation and Classification Using Entropy-Based Convolutional Module

HWA-RANG KIM[1,2], KWANG-JU KIM[2], (Associate Member, IEEE), KIL-TAEK LIM[2], AND DOO-HYUN CHOI[1]

[1]Graduate School of Electronic and Electrical Engineering, Kyungpook National University, Daegu 41566, South Korea
[2]Electronics and Telecommunications Research Institute, Daegu 42994, South Korea

Corresponding authors: Kwang-Ju Kim (kwangju@etri.re.kr) and Doo-Hyun Choi (dhc@ee.knu.ac.kr)

This work was supported in part by the Electronics and Telecommunications Research Institute (ETRI) Grant through the Korean Government (Development of ICT Convergence Technology for Daegu-GyeongBuk Regional Industry) under Grant 21ZD1100, and in part by the Seoul National University Hospital through the Korea Health Technology Research and Development Project by the Korea Health Industry Development Institute (KHIDI) by the Ministry of Health and Welfare, Republic of Korea, under Grant HI18C0316.

ABSTRACT As the powerful performance of deep learning has been proven, many computer vision researchers have applied deep learning methods to their works as a breakthrough that could not be achieved with conventional computer vision algorithms. Particularly in pathological image analysis, deep learning plays an important role because some diagnosis requires a considerable cost or much time. In a recent, convolutional neural network (CNN)-based deep learning models have shown meaningful results in pathological image analysis, reducing time and cost. However, existing CNN-based segmentation models perform the same convolution operation for all channels of a feature map. It could be an inefficient operation according to information theory. We propose (Shannon) entropy-based convolutional module (ECM) for efficient convolutional operation in terms of a communication system. The fundamental coding manner of a communication system based on information theory is to allocate fewer bits for data showing the high probability of occurrence, and vice versa. Following up this coding manner, a feature is divided into dominant and recessive features according to the channel importance calculated from the channel attention module, and a heavy operation is conducted on the recessive feature and a light operation is conducted on the dominant feature. This operating manner can make a network perform efficient calculations and improve its performance. Furthermore, our proposed module is a portable unit, thus it can be a replacement of any convolution without modification of the whole architecture. To the best of our knowledge, our proposed module is the first trial to mimic the coding manner of information theory. The models equipped with our proposed module outperform the original models achieving 0.855 of F1 score and 0.832 of Jaccard score on colorectal cancer (CRC) image data-set.

INDEX TERMS Segmentation, deep learning, information theory, Shannon entropy, colorectal cancer image.

I. INTRODUCTION

Automatic algorithms for pathological image classification and segmentation occupy a large part of computer-aided diagnosis (CAD). CAD is the use of an output generated by a computer as an assisting tool for a clinician. This clinician makes the final diagnosis to make an accurate decision. But CAD can be a great tool to help clinician find candidates for affected areas. From the earliest, many researchers have tried numerous image segmentation or classification task with statistical approaches for sophisticated CAD [1]–[4].

Over the past few years, however, deep learning methods have shown outstanding performance and yielded novel image segmentation models. Deep learning models can solve many image understanding problems highly complicated to analyze by training deep neural layers. This is because a neural architecture provides suitable constraints for a data-set by iterative training process. This excellence of deep learning

The associate editor coordinating the review of this manuscript and approving it for publication was Kumaradevan Punithakumar.

made many researchers shift their study field to deep learning, and clinicians and engineers have begun to collaborate to analyze medical images.

We develop a histological image segmentation and classification model to work on the CRC image data-set to contribute above works (CRC is an alarming threat to health in cancer-related deaths in many countries).

To determine if a patient responds to immunotherapy, a microsatellite instability (MSI) index is diagnosed based on a medical expert's experience. The MSI status classes have MSI-High (MSI-H) and MSI-Low (MSI-L) or MSI-Stable (MSS). Figure 1 shows samples of CRC images and masks. White spaces of masks are mapped to the tumor regions, classified as MSI-H or MSI-L (MSI-L and MSS are the same class). Non-masked regions contain no MSI status, which means they are all normal tissues.

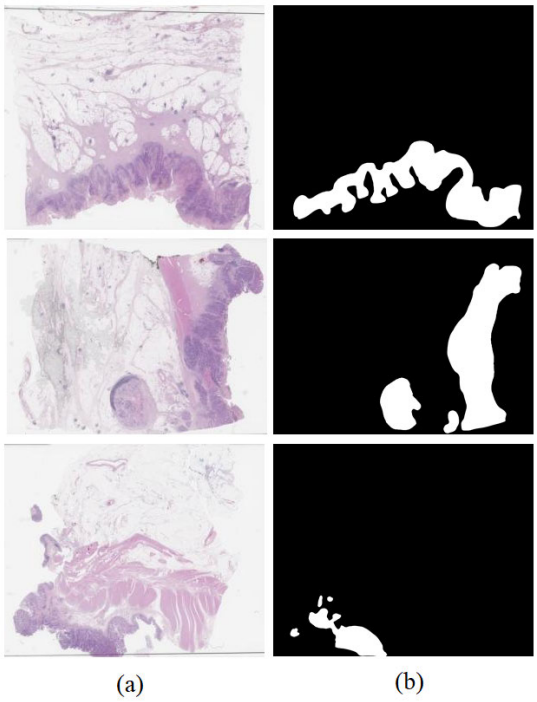

FIGURE 1. Samples of the CRC data-set. (a) CRC images (b) corresponding masks.

The pathological reporting of MSI status is strongly recommended for all surgically resected CRC cases. A general diagnosis procedure is conducted by examining Hematoxylin and Eosin (H&E) stained CRC tissue and manually checking abnormalities in microscopic images. However, this procedure is tedious and sometimes prone to error. Pathological image-based automatic diagnosis methods with deep learning approaches could reduce the fatigue of pathologists.

However, deep learning still has poor functionality when it comes to being considered as one of the communication systems that transmit data. Figure 2 shows brief diagrams of a communication system and a typical segmentation model. In a communication system, information is to be transmitted.

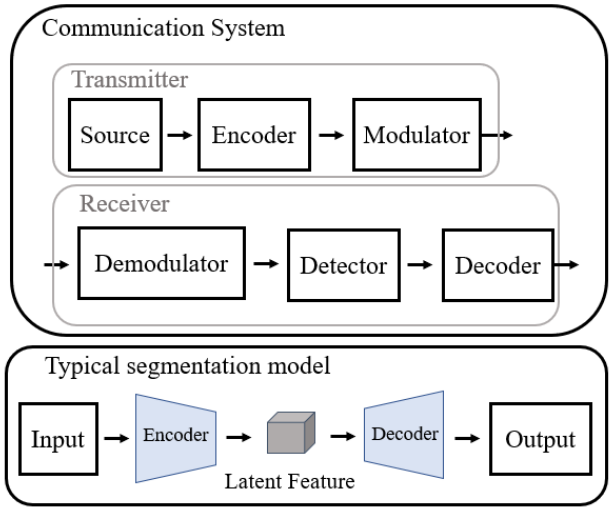

FIGURE 2. Brief diagrams of a communication system and a typical segmentation model. Two systems have similar concept in terms of data transmission.

Signals of information are the single-valued function of time that carries the information, and it is converted into an electrical form for transmission.

In reality, however, many things have to be considered for transmission: Signal should be amplified to keep signal strength and modulated to be transmitted over a large distance. Further, to satisfy the theoretical condition, hardware design must be sophisticated. Of course, a deep learning architecture is not related to those real problems, it can be thought of as a communication system because the information is conveyed through hidden layers.

The important commonality between a communication system and a deep learning model is encoding process. Although in a communication system, encoding is not necessary, it can provide significant efficiency for transmission. Likewise, in a deep learning model, it is not easy to make efficient predictions without encoding. Figure 3 shows the compression coding manners of a communication system and a neural network. For the 6 symbols to convey, general code allocates 3 bits for the expression of the symbols. For more efficient data transmission, however, the compressed code (Shannon-Fano coding [5]) allocates various lengths of bits (the expected bit length of the general code is 3, the compressed code is 2.44). This coding manner is based on information theory which has been initially proposed by Shannon [6]. The main principle of information theory is that the lower probability of occurrence, the more information data have. Thus, few bits are needed to transmit data that has a higher probability, many bits are needed to transmit data that has a lower probability.

This paper proposes the ECM based on information theory to mimic the coding manner of a communication system. For the features which have a higher probability, the ECM will apply a small amount of convolutional operations, for the features which have a lower probability, the ECM will apply a large amount of convolutional operations.

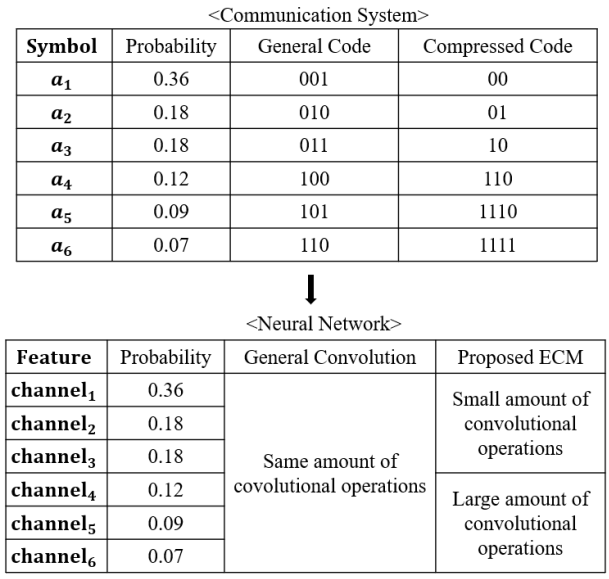

FIGURE 3. The motivation of the proposed ECM. Our module mimics the concept of a communication system. According to channel probability(intensity), different convolutional operations are applied. Specifically, for channels that have a large probability, small amount of convolutional operations are applied because the channels have small amount of information to be extracted.

In summary, the main contributions of this paper lie in three aspects:

- Our proposed ECM can be a replacement for a vanilla convolution. Therefore, the ECM can be used for any type of structure that contains CNN modules.
- To the best of our knowledge, our proposed ECM is the first trial to mimic the coding manner of information theory.
- Our proposed ECM improves the performance of well-known architectures without modifications of the model architectures. We achieve 0.855 of F1 score and 0.832 of Jaccard score on the CRC image data-set.

The remainder of this paper is organized as follows. Section II describes a brief overview of the background and related works in semantic segmentation based on deep learning. Section III presents the proposed ECM. The experimental process and results are described in section IV, and section V describes the conclusion.

II. RELATED WORKS

Before the deep learning boom, many researchers have tried to perform image segmentation tasks with conventional approaches. Soo-Hee Han *et al.* proposed memory-efficient approaches for the segmentation of airborne laser point clouds [7]. Though it works with mathematical and geometric approaches, the model is not enough to cover the diversity of target shapes because it does not have enough non-linearity. However, as deep learning-based methods emerged, the problem began to be solved. As time goes by, deep learning skills have become more refined, and many models have proven their excellence. Among many deep learning models, some models play an important role as cornerstones. From the underlying contribution, many approaches for pathological image analysis have also been proposed. In this section, prominent deep learning-based segmentation models are introduced.

A. FULLY CONVOLUTIONAL NETWORK

Since Long *et al.* [8] proposed a fully convolutional network (FCN), there has been a remarkable improvement in segmentation performance, which removes fully connected layers to preserve local information. FCN includes only convolution layers, making it possible to take an arbitrary size of the image. FCN is based on CNN architectures such as VGG16 [9] and GoogLeNet [10], but others can replace such backbones for better feature extraction. Further, the output map can be adjusted to any size because there are no fully connected layers.

FCN uses skip connections in which feature maps from the final layers are up-sampled and fused with feature maps of earlier layers to capture multi-scale information. The flexible and refined architecture enables the model to produce a detailed segmentation map. FCN is a great cornerstone in image segmentation, providing end-to-end training for segmentation on the random-sized image.

B. ENCODER-DECODER ARCHITECTURES

After the FCN, many architectures based on encoder-decoder architecture are introduced. Noh *et al.* [11] proposed deconvolution network for semantic segmentation. The deconvolution network's decoder is composed of an un-pooling layer and deconvolution, which predict segmentation masks. Badrinarayanan *et al.* [12] proposed the SegNet which is similar to deconvolution network. The key idea of the SegNet is the up-sampling way of the decoder. It uses pooling indices already computed in encoding stage, enabling the model to perform non-linear up-sampling.

The HRNet [13], a high-resolution network, maintains high-resolution features by using connections between high and low resolution feature maps in parallel. This HRNet has strength for understanding multi-scale objects in images.

The DeepLab series proposed by Liang-Chieh Chen *et al.* also can cover the variable size of objects by using atrous convolution. Liang-Chieh Chen *et al.* first proposed DeepLabV1 [14] and DeepLabV2 [15]. Both architectures adopt atrous convolution and a fully connected conditional random field (CRF) which helps the decoder make a refined segmentation mask. DeepLabV2 has one more module named atrous spatial pyramid pooling (ASPP). ASPP is an atrous version of SPP, which is introduced in SPP-Net [16]. In ASPP, atrous convolutions with different rates are applied to the feature map and fused. DeepLabV3 [17], which outperforms PSPNet [18], handles the problem of segmenting objects at multiple scales and its extended version is DeepLabV3+ [19]. DeepLabV3+ has a useful decoder module to refine the segmentation mask, resulting in a fast and robust encoder-decoder network. Soo-Hee Han *et al.* applied those general architectures and developed them.

C. MEDICAL IMAGE SEGMENTATION

For broader and faster diagnosis of medical images, engineers have tried to adapt deep learning models to medical image analysis [20], [21]. The U-Net [22], which consists of contracting and expanding paths, has shown outstanding biomedical image segmentation performance. The contracting path which can be called encoder reduces the spatial dimension to save operating cost while the expanding path which can be called decoder recovers dimension and detail for generating output segmentation mask. Moreover, the U-Net uses skip-connection between encoder and decoder to prevent spatial information's disappearance during the encoding stage.

For more robust architecture, Zongwei Zhou *et al.* proposed the UNet++ [23], which has a nested and dense connection between encoder and decoder. In the U-Net, skip connection is just a concatenation of the encoder feature and decoder feature, but the UNet++ changes this connection to the convolution module. This architecture achieves higher accuracy than the original U-Net because the nested convolution path can preserve better feature localization.

Bo Wang *et al.* proposed the dual encoding U-Net [24], which has two encoders: spatial path and context path. They help networks preserve spatial information and semantic information. However, the model parameter number is too big. Thus it demands a large amount of computing power.

Ricardo *et al.* proposed cascaded architecture [25] using variational auto-encoder [26] which is cascaded after the segmentation network to improve the topological coherence. Pengshuai Yin *et al.* proposed PM-Net [27], based on Mask-RCNN [28]. PM-Net has a segmentation-based region proposal network and pyramid RoIAlign module to aggregate the multi-level information to better feature representation. Yicheng Wu *et al.* proposed Vessel-Net [29] for retinal vessel segmentation. It is designed with an efficient inception-residual convolutional block to combine the inception and residual modules' advantages. Kehan Qi *et al.* proposed X-Net [30] to address the problem that model performances are limited due to the insufficient training of a large number of parameters, which sometimes fail in capturing long-range dependencies. X-Net is based on depth-wise separable convolution, allowing to reduce the network size. Yalong Liu *et al.* proposed Refined Segmentation R-CNN [31], which is a lightweight segmentation network for biomedical image segmentation. The network embeds a heuristic region proposal network that can utilize surrounding information for heuristic segmentation.

Unlike the models described above, conditional random field and graph-based neural network have been utilized for medical image processing in other researches [32]–[35]. To analyze complex images, the spatial relationship between image locations is extracted by conditional random field or graph-based neural network. Dan Xue *et al.* proposed a novel ensembled transfer learning technique [36]. In this technique, the features from various extractors are processed by weighted voting for ensemble learning. This technique can aggregate the feature extraction capabilities of multiple extractors. Jun Xu *et al.* first reported on the development of computerized spermatogenesis staging (CSS) based on quantitative image analysis that outperforms a human histologist [37].

In this paper, we suggest an improvement that all the models described above did not consider. We propose the ECM to mimic the fundamental coding manner of information theory, carrying out an efficient feature extraction.

III. METHOD

In this section, the analysis strategy for the CRC image data-set is described. We propose ECM, which is based on Shannon entropy. The ECM can be used as a plug-and-play module without modifying the entire model, increasing model performance.

A. QUANTITIES OF INFORMATION

This paper mainly deals with a deep learning methodology in terms of information theory. Information theory concerns measures of information of the distributions associated with random variables. The quantities of information in a random variable are calculated as eq. (1) to deal with information.

$$I(x) = -log_2 P(x) \tag{1}$$

The quantities of information are based on the probability of random variable (probability of random variable $P(x)$ is distributed between 0 and 1). The higher the probability of occurrence, the lower the amount of information. Based on the probability mass function, the Shannon entropy is given by eq. (2).

$$H = -\sum_{i}^{n} p_i log_2(p_i), \tag{2}$$

where p_i is the probability of occurrence of the i-th value, n is the number of samples.

B. ENTROPY-BASED CONVOLUTIONAL MODULE

To mimic information theory in terms of data transmission, we propose an ECM-based image segmentation model. Figure 4 shows the architecture of the ECM. First, a channel sorting module (CSM) which is described in Algorithm 1 is applied to the input feature map. CSM aims to sort feature maps according to the intensity of the channel attention vector. The channel attention vector is generated by the channel attention module introduced in [38]. Figure 5 shows the channel attention module. The module utilizes both max-pooling outputs and average-pooling outputs with a shared network. And then two vectors are summed and pass through an activation function, creating a channel-wise attention vector. This channel attention vector implicitly means the intensity of each channel. The intensity has the same meaning as the probability in Figure 3. The intensity value of a channel attention vector tends to be large when a feature has important information of an image, meaning that the feature often appears, hence it can be thought of as a probability.

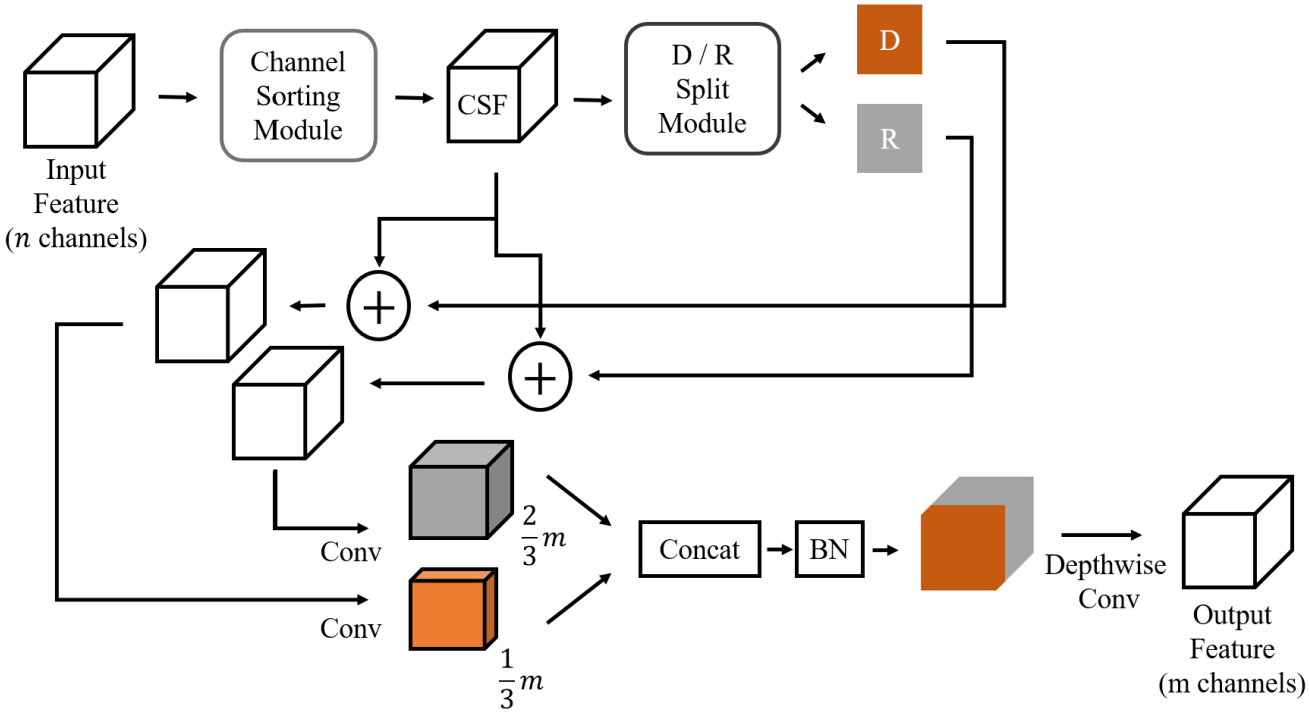

FIGURE 4. The proposed ECM. The ECM follows the coding manner of a communication system. For the channels which have large intensity, a small amount of convolutional operations are applied, and vice versa. Specifically, channels of input feature map are sorted according to their intensities calculated by the channel attention module shown in Figure 5. After that, channels are split according to the threshold as shown in Figure 6. These split features represent a dominant and recessive feature, and each feature has a different amount of information. And then the dominant feature becomes $1/3 * m$ channel, the recessive feature becomes $2/3 * m$ channel, where m is output channel. The two feature maps are concatenated, and batch normalization and depthwise convolution are applied.

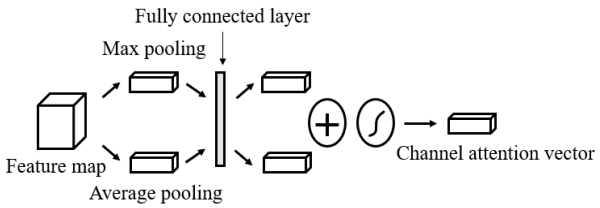

FIGURE 5. The channel attention module. The generated channel attention vector presents the probability values of each channel and has the same length with the channel of the feature map [38].

Algorithm 1 CSM(Channel Sorting Module)

1: *input* ← feature map
2: *index* ← channel attention vector of *input*
3: Sort the *input* channel according to *index*
4: **return** channel sorted feature

After generating the channel attention vector, channels are sorted according to the channel attention vector's value (the sorted feature is easier to be utilized at the next operation). The rearranged feature map is called the channel sorted feature (CSF) in this paper.

After the CSM operation, CSF goes through the dominant/recessive split module (DRSM) which is described in Algorithm 2. Figure 6 shows the DRSM that separates the feature map into the dominant/recessive feature according to

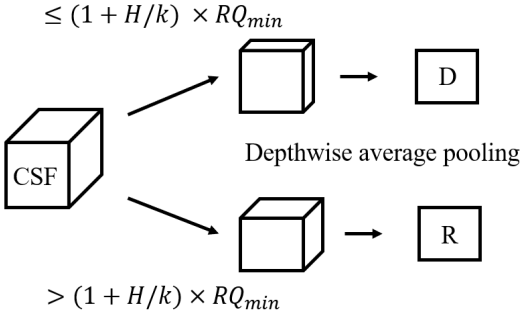

FIGURE 6. Dominant/recessive split module. From the CSF, channels which have smaller RQ go into *D*, and vice versa.

the threshold. To set the threshold, we first define the relative quantity (RQ) as in eq. (3).

$$\mathrm{RQ}(x) = \frac{I(x)}{H} \tag{3}$$

The feature map is divided into the D feature (dominant feature) and the R feature (recessive feature) by the criterion decided by the minimum value of RQ, entropy H and hyperparameter k. Channels whose RQ value is smaller than $(1 + H/k)$ times the value of minimum RQ go into D feature, other channels go into R feature (See Figure 6). Then each feature is downsized with depthwise average pooling shown in Figure 7. Depthwise average pooling produces

Algorithm 2 DRSM(Domain/Recessive Split Module)

$threshold \leftarrow (1 + H/k) * \mathrm{RQ}_{min}$
$CSF \leftarrow Channel\ sorted\ feature$
for $i = 1, 2, \ldots,$ *channel length* **do**
  if *Channel intensity* $> (1 + H/k) * \mathrm{RQ}_{min}$ **then**
    Append $CSF[i]$ to R
  else
    Append $CSF[i]$ to D
  end if
  $D \leftarrow depthwiseAvergePooling(D)$
  $R \leftarrow depthwiseAvergePooling(R)$
end for
return D, R

one channel feature map from an arbitrary number of channels, enabling the model to train the DRSM. Because the entropies are changed for every iteration, the fixed kernel cannot be adapted to generate one channel feature for every batch. On the contrary, depthwise average pooling enables the model to be trained by making the channel's arbitrary number into one channel.

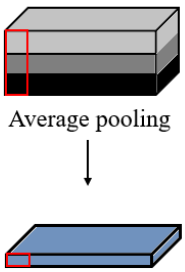

FIGURE 7. Brief diagram of depthwise average pooling. Unlike normal average pooling, it calculates the average value of channels.

The D and R are then added to CSF as shown in Figure 4. After that, convolutions are applied to each D and R feature map. For the D, the output channel becomes $m/3$, and for R, the output channel becomes $2 * m/3$, where m is the number of the final output channel. This is because the D has less information than the R (more convolutional non-linearity is needed to extract information from the R feature). Note that this is the coding scheme of the ECM.

Then, the two feature maps are concatenated, resulting in an m channel feature map. Finally, the depthwise convolution shown in Figure 8 is applied to extract latent features from the previous feature map at a low cost. The process of the ECM is described in Algorithm 3.

The advantage of our proposed module is that users can replace a convolution with our module very easily, increasing performance. Our module can extract features efficiently by applying different amounts of convolutional operations. However, our module needs to set the hyperparameters, and optimal hyperparameters for a data-set should be found by empirical tests.

Algorithm 3 ECM

$m \leftarrow output\ channel$
$CSF \leftarrow CSM(input)$
$D, R \leftarrow DRSM(CSF)$
$DCSF \leftarrow Convolution(CSF + D)$
$\{DCSF\ has\ 1/3 * m\ \text{channels}\}$
$RCSF \leftarrow Convolution(CSF + R)$
$\{RCSF\ has\ 2/3 * m\ \text{channels}\}$
$concat\_f \leftarrow concat(DCSF, RCSF)$
$output \leftarrow DepthwiseConvolution(BN(concat\_f))$
return *output*

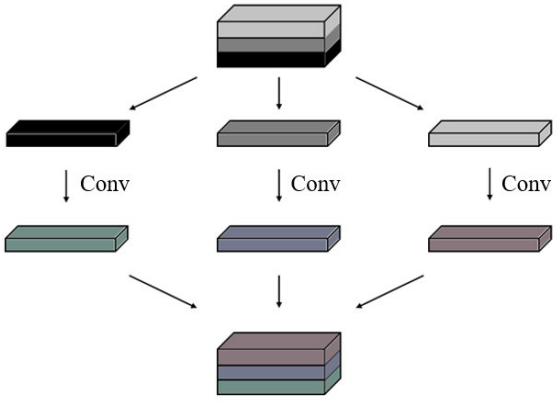

FIGURE 8. Brief diagram of depthwise convolution. It extracts spatial information from each channel.

C. ECM-EQUIPPED NETWORKS

Our proposed ECM can be used in any architecture including convolution layers. We use ResNet50 [39], which is still recognized for its outstanding performance as the backbone. Figure 9 shows diagrams of the original residual bottleneck block and the ECM-equipped residual bottleneck block. The ECM-ResNet, used in the experiment, is designed by

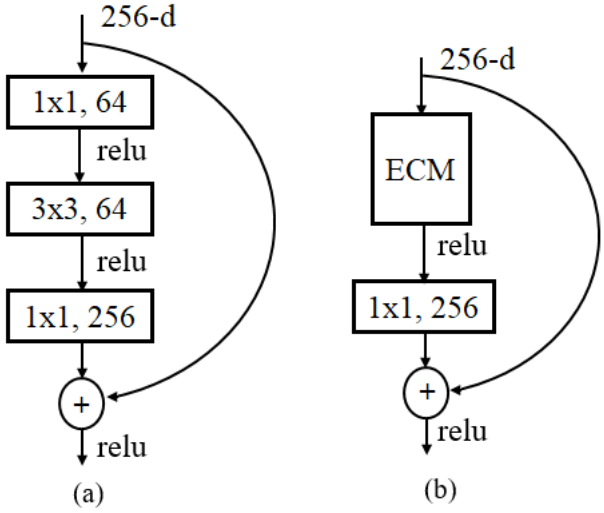

FIGURE 9. A comparison of two residual blocks. (a) The original residual bottleneck block (b) The ECM-equipped residual bottleneck block.

replacing the residual bottleneck block with the ECM-equipped residual bottleneck block.

Figure 10 shows the architecture of the ECM-equipped DeepLabV3+ used in the experiment. The backbone network is the ECM-ResNet, and the last convolution layer is replaced with the ECM in the decoder. ASPP is not replaced with the ECM to keep its functionality to capture multi-scale feature information with atrous convolution.

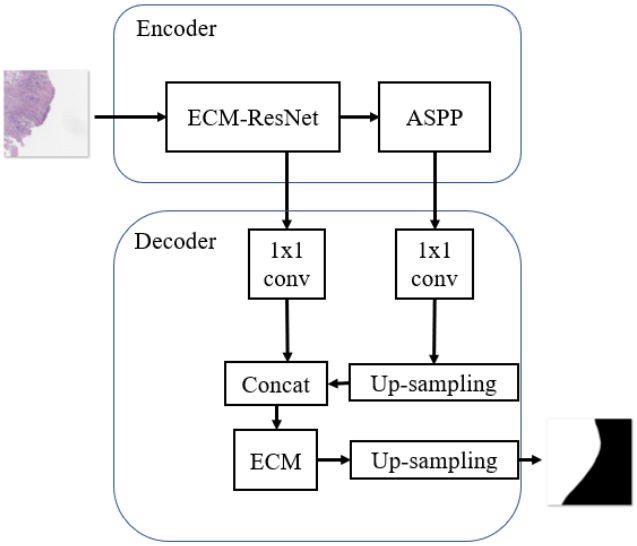

FIGURE 10. The architecture of the ECM-equipped DeepLabV3+. The backbone is the ECM-ResNet, and the convolution before the last up-sampling is replaced by the ECM.

Like the ECM-equipped DeepLabV3+, other segmentation models can equip the ECM. In this paper, PSPNet, U-Net, UNet++ are modified and tested. Figures 16 to 18 in the appendix illustrate the modified models.

IV. EXPERIMENTS

A. DATA DESCRIPTION

Typically, biomedical images are collected as a whole slide image (WSI) with an enormous size of pixels. The WSIs are originally provided with SVS format and each has about 3GB of capacity corresponding to 90,000 ∼ 120,000 pixel-size. All WSIs were scanned at 40× magnification.

In this experiment, a WSI is divided into small tile images in which size is [3,512,512] (3 RGB channels) because of the computing source's limitation. After tiling, we gain 5,000 training images. Among those, 1,000 images are used for validation and the test data-set consists of 1,746 tile images. Output segmentation mask size is the same as input image size.

Figure 11 shows a tile image and segmentation mask. The white space is a tumor area that can be classified as MSI-H or non-MSI-H. There are no cases in that one image has two classes. If a tile image is annotated as MSI-H, all white space in the image is MSI-H tumor area.

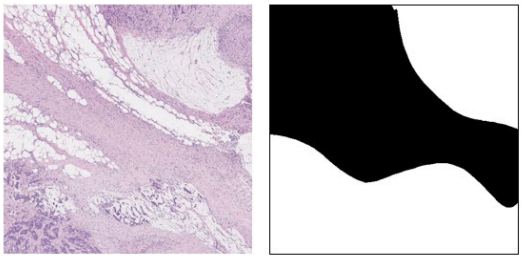

FIGURE 11. A sample of tile image. (a) a tile image (b) segmentation mask.

B. EVALUATION METRICS

CRC images are collected to predict MSI status and check the tumor area of the affected part. There are two evaluations: 1) MSI status classification task. 2) the segmentation task. The classification task is evaluated by F_1 score calculated by eq. (4).

$$F_1 = 2 * \frac{precision * recall}{precision + recall} \tag{4}$$

Precision is calculated by TP/(TP + FP) and recall is calculated by TP/(TP + FN), and TP, TN, FP, FN are described in Table 1. For example, if a prediction and a ground truth are the same and positive, then the prediction is true positive. The F1 score is calculated based on MSI-H. MSI-L or MSS are treated as background.

TABLE 1. Confusion matrix of MSI-H prediction.

	Ground truth	
Prediction	**MSI-H**	**non-MSI-H**
MSI-H	True Positive(TP)	False Positive(FP)
non-MSI-H	False Negative(FN)	True Negative(TN)

The segmentation task is assessed by Jaccard-score calculated by eq. (5). It is the same as IoU(Intersection over Union) that quantifies the percent overlap between target and prediction. $|X \cap Y|$ means an intersection between target and prediction, $|X \cup Y|$ means a union. Thus, it is a method of measuring how well two areas overlap.

$$J(X, Y) = |X \cap Y|/|X \cup Y| \tag{5}$$

C. CLASSIFICATION TASK

There is no classification branch in our models. Thus classification result comes from the segmentation result map. For example, if MSI-H class is dominant in a segmentation map, then the image is classified as MSI-H, and vice versa.

D. TRAINING DETAIL

In this experiment, all models are trained from scratch with Adam optimizer [40]. The learning rate is 0.0001 and the cosine annealing scheduler is adopted to find several

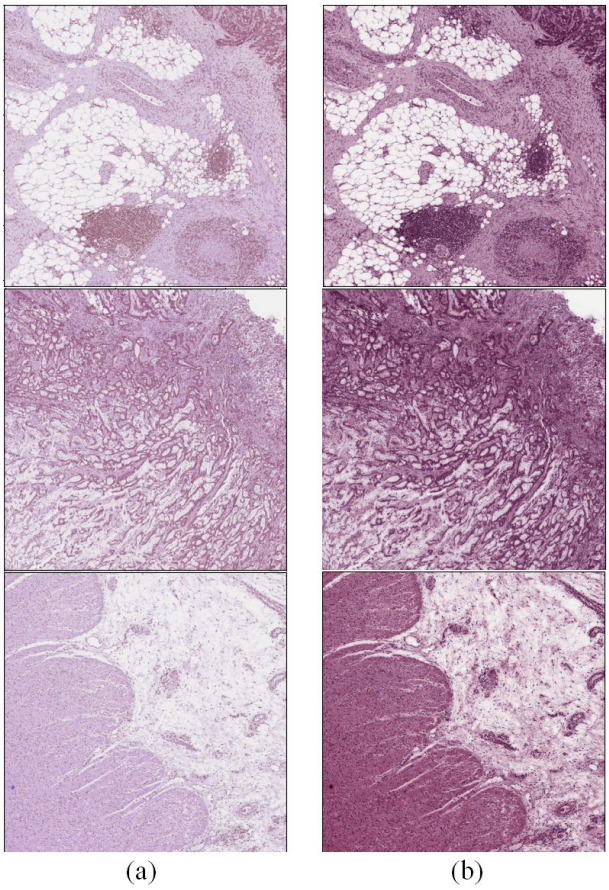

FIGURE 12. Samples of stained images and stain normalized images. (a) H&E stained images (b) stain normalized images.

optimization points iteratively. And the loss function is cross-entropy function, which is calculated by eq. (6).

$$CE(p, q) = -\sum_{i} p(i) \log q(i) \tag{6}$$

The maximum training epoch is set by 200, but every training was converged under 100 epochs. All kernels in the models are initialized with He initialization [41]. The training and testing are conducted on NVIDIA GeForce GTX TITAN XP GPU with 12GB memory.

E. H&E STAINING NORMALIZATION

Histological sections should be stained because most cells are transparent. Among staining skills, the most commonly used thing is H&E staining. However, images can be over-stained or weakly stained, causing wrong stained pixels.

In this experiment, we adapt three normalization methods introduced in [42]–[44] to reduce the variability of images. Among the normalization methods, we mainly utilize the method of [42] considering that the method is simple and widely used. Further, there is not much difference in performance compared to the other methods. The results for [43], [44] will be described in ablation study section.

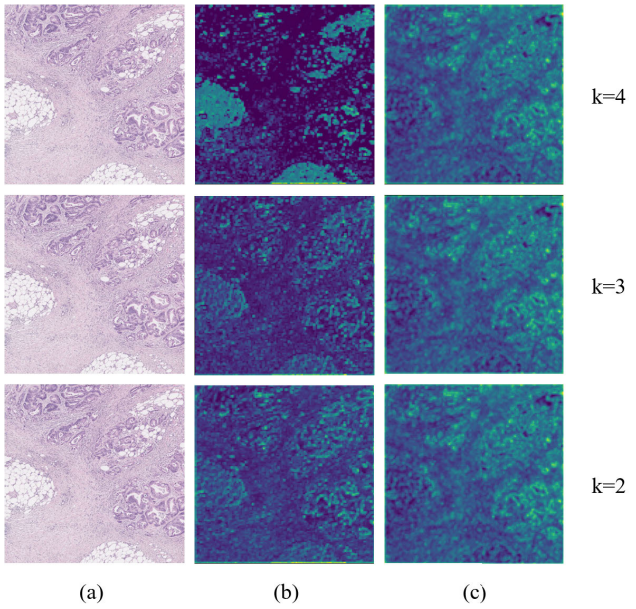

FIGURE 13. A comparison of the features according to k. (a) original images (b) dominant features (c) recessive features.

Figure 12 shows the H&E stained images (left column) and staining normalized images (right column) by adapting the method of [42]. In this experiment, H&E staining normalization increases accuracy slightly.

F. PERFORMANCES

We conduct CRC image segmentation and classification with the PSPNet, U-Net, UNet++, and DeepLabV3+. Table 2 shows the result comparison between original networks and ECM-equipped networks. We implement three types of experiments, setting different k. For all the models in this experiment, the best performance is shown when $k = 4$.

Among the models, the ECM-equipped DeepLabV3+ shows the best performance with 0.855 of F1 score, 0.832 of Jaccard score. Figure 14 shows the segmentation results of the ECM-equipped DeepLabV3+ on the CRC images.

G. ABLATION STUDY

This section describes ablation studies to confirm how to set the hyperparameters and conduct experiments on another data-set. All experiments in this section use the ECM-equipped DeepLabV3+ that shows the best performance on the previous tests, and hyperparameter k is set to 4.

1) REVERSE-ECM

To confirm the effectiveness of the proposed ECM, we conduct an ablation study. We test the reverse version of the ECM in which dominant features go into $2 * m/3$ channels, and recessive features go into $m/3$ channels contrary to the ECM shown in Figure 4. Table 2 shows the results of the reverse-ECM. As shown in the Table, the reverse-ECM models show little higher or little lower performance than originals. This is

TABLE 2. Results of original models and ECM-equipped models. The ECM-equipped models outperform the originals entirely except recall score of U-Net++.

	F_1 Score			Jaccard Score			Precision			Recall		
Model	k=4	k=3	k=2	k=4	k=3	k=2	k=4	k=3	k=2	k=4	k=3	k=2
PSPNet		0.658			0.642			0.605			0.722	
U-Net		0.622			0.706			0.557			0.706	
U-Net++		0.717			0.730			0.705			0.731	
DeepLabV3+		0.789			0.765			0.735			0.852	
PSPNet + ECM	0.672	0.657	0.648	0.708	0.701	0.709	0.623	0.611	0.587	0.731	0.712	0.725
U-Net + ECM	0.684	0.679	0.646	0.711	0.708	0.690	0.619	0.603	0.593	0.765	0.777	0.710
U-Net++ + ECM	0.722	0.691	0.692	0.734	0.722	0.711	0.735	0.720	0.732	0.678	0.666	0.657
DeepLabV3+ + ECM	**0.855**	0.823	0.844	**0.832**	0.801	0.808	**0.788**	0.753	0.777	**0.935**	0.908	0.925
PSPNet + Reverse-ECM	0.661	0.625	0.632	0.653	0.655	0.636	0.612	0.593	0.599	0.718	0.627	0.668
U-Net + Reverse-ECM	0.625	0.613	0.608	0.698	0.687	0.690	0.622	0.589	0.591	0.628	0.639	0.645
U-Net++ + Reverse-ECM	0.702	0.689	0.711	0.735	0.725	0.722	0.682	0.673	0.701	0.723	0.705	0.721
DeepLabV3+ + Reverse-ECM	0.778	0.773	0.765	0.774	0.767	0.762	0.756	0.744	0.732	0.801	0.804	0.802

TABLE 3. Results for the other criterions. We test three other criterions, but they all show lower performance than the previous defined criterion.

Criterion for dominant feature	F_1 Score	Jaccard Score	Precision	Recall
$\text{RQ} < k * \text{RQ}_{min}$	0.566	0.322	0.510	0.635
$\text{RQ} < k + \text{RQ}_{min}$	0.677	0.603	0.623	0.741
$\text{RQ} < (H/k) * \text{RQ}_{min}$	0.811	0.803	0.788	0.835

TABLE 4. Results for the other components. Among the components, the normalization method of [44] shows better performance than the previous method, but it is very minimal. Thus, we utilize the previous method considering its simplicity.

Changed Component	F_1 Score	Jaccard Score	Precision	Recall
256x256	0.823	0.809	0.756	0.903
HSV	0.844	0.811	0.761	0.947
Normalization method of [43]	0.830	0.819	0.759	0.915
Normalization method of [44]	**0.858**	**0.844**	**0.791**	**0.937**

because the reverse-ECM does not follow the coding manner of information theory.

2) HYPERPARAMETER *k*

Figure 13 shows dominant features and recessive features along with k. The dominant feature at $k = 4$ is the clearest, and the feature at $k = 2$ is the most blurry. Models at $k = 4$ best follow our intention to split dominant and recessive features and show the highest performances.

Further, we conduct a modified version of the ECM in which the inequality in Figure 6 is changed as shown in Table 3. Simply multiplying k does not work, because entropy values of feature maps are different for each batch. Simply adding k works better but still not meaningful. When H/k is multiplied to RQ_{min}, it shows better performance than just multiplying k. This is because H/k represents the relative value of entropy for every batch. However, if H/k is under 1, there is no dominant feature, and this causes performance degradation. This is why we set $1 + H/k$ for the criterion. Finally, we conduct the experiments with setting $k = 1$ or $k = 5$, but they show worse performance than the original models.

TABLE 5. Results for the other channel dimensions. m is channel of output feature (see Figure 4). Among the tested channels, $m/4$ and $m * 3/4$ channel shows close performance to $m/3$ and $m * 2/3$ channel. With these empirical tests, we can guess the optimal setting is near $m/3$ and $m * 2/3$.

channel	F_1 Score	Jaccard Score	Precision	Recall
$m/2$ and $m/2$	0.787	0.783	0.735	0.846
$m/4$ and $m * 3/4$	0.829	0.793	0.779	0.885
$m/5$ and $m * 4/5$	0.799	0.771	0.740	0.868

3) EXPERIMENTS FOR OTHER COMPONENTS

We analyze for other color model, image size, and stain normalization methods. First, we resize the images to 256×256, but it shows lower performance than the previous experiment (512×512).

Second, we change the color model to HSV (Hue, Saturation, Value). It also shows lower performance than the previous experiment (RGB).

Third, we change the stain normalization method. We utilize the stain normalization methods proposed by Reinhard *et al.* [43] and Vahadane *et al.* [44]. As result, the method proposed by Vahadane *et al.* shows a higher performance, but it is very minimal. Moreover, the staining normalization method of [42] is easier to be utilized and simple, hence our main experiments are performed using the method [42] shown in figure 12. Figure 19 in the appendix shows the images normalized by the other methods.

The experiments are conducted with the ECM-equipped DeepLabV3+ that shows the best performance on the previous experiment. The results are shown in Table 4.

4) EXPERIMENTS FOR OTHER CHANNEL DIMENSIONS

As shown in Figure 4, our module applies different convolutional operations for a dominant and recessive feature. However, it is hard to find the optimal amount of convolution among infinite number of cases, but we provide a rough guideline by conducting empirical tests. We additionally conduct for three kinds of convolution that bring out $m/2$ and $m/2$, $m/4$ and $m * 3/4$, $m/5$ and $m * 4/5$ channels. Table 5 shows the results, the best score is still from the

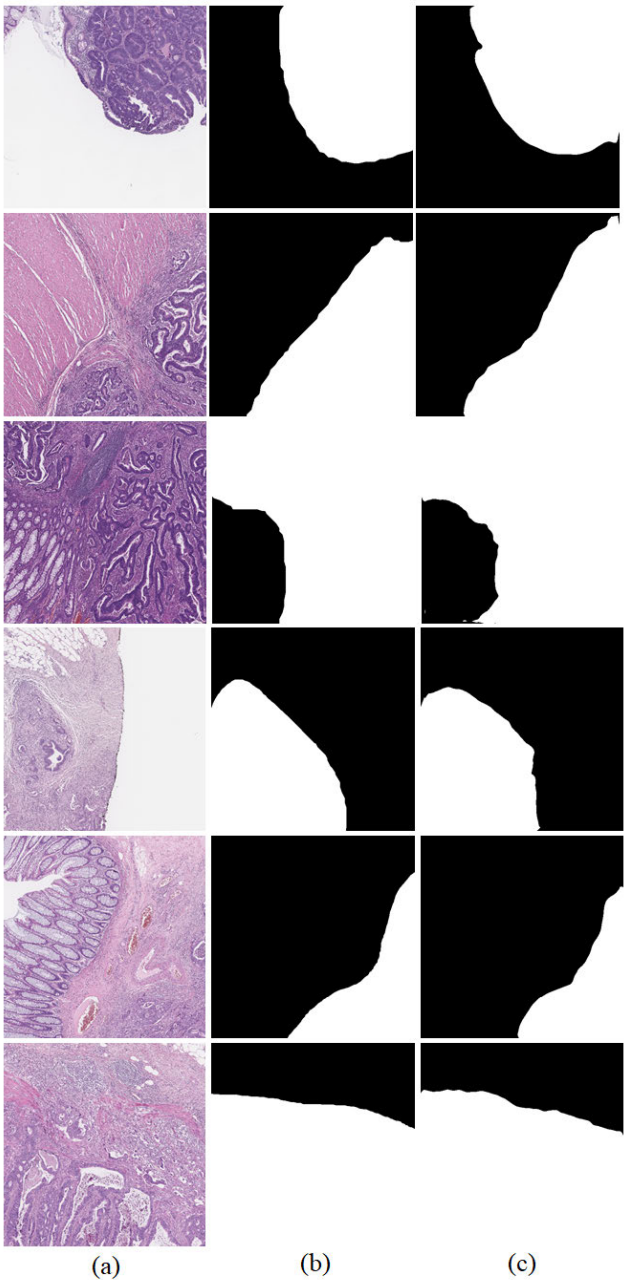

FIGURE 14. Segmentation results of the ECM-equipped DeepLabV3+ which shows the best segmentation performance among the tested models. (a) input H&E stained images (b) labels (c) predictions.

original experiment in Table 2, but we can observe that a bigger gap than a certain amount leads to performance degradation. And the same amount of convolution, $m/2$ and $m/2$, is worse than the others. From this experiment, at least for the CRC data-set, we can guess that the optimal setting is near $m/3$ and $m * 2/3$.

5) EXPERIMENT ON ANOTHER DATA-SET

We conduct an additional experiment on low grade glioma (LGG) segmentation data-set obtained from The Cancer Imaging Archive (TCIA) [45]. LGG is a brain tumor more likely developed when someone is exposed to radiation. We experiment with the ECM-equipped DeepLabV3+, which showed the best performance on the CRC data-set.

TABLE 6. Results for LGG data-set. Our proposed module shows performance improvement for the data-set.

Model	F_1 Score	Jaccard Score	Precision	Recall
DeepLabV3+	0.903	0.856	0.877	0.908
DeepLabV3+ + ECM	**0.932**	**0.897**	**0.898**	**0.967**
DeepLabV3+ + Reverse-ECM	0.912	0.867	0.886	0.919

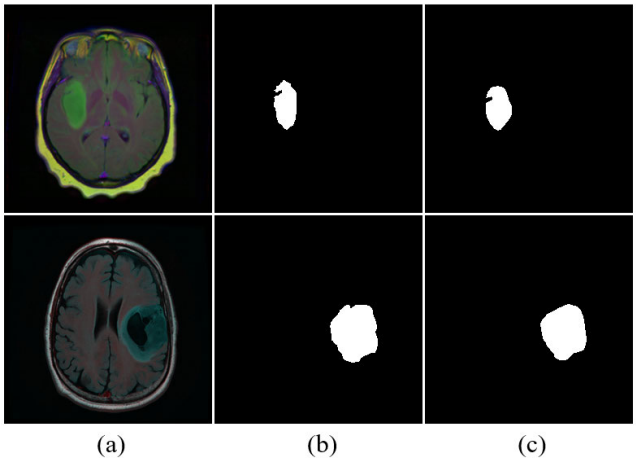

FIGURE 15. Segmentation results of the ECM-equipped DeepLabV3+ on the LGG images. (a) input images (b) labels (c) predictions.

An LGG image is [3, 256, 256] shaped (3 RGB channel) and has 2 classes: tumor exists or not. Thus, if a segmentation result map pixel is all zero, then it is classified non-tumor, and vice versa.

We experiment with 3,000 training images and 900 test images. Training detail is the same as the CRC experiment. As shown in Table 6, the ECM-equipped DeepLabV3+ performs the best score. Figure 15 shows the segmentation results on the LGG images.

V. CONCLUSION

We propose a novel entropy-based convolutional module that can be adapted to CNN architectures, increasing performance. The ECM is based on information theory that gives great reference to build a model for efficient data transmission. Unlike conventional models, our proposed module performs differentiated operations by calculating the amount of information in the feature for each batch. This modular design enables efficient computation of feature extraction. Further, our module can be a replacement for vanilla convolution, and to the best of our knowledge, our module is the first trial to mimic the coding manner of information theory.

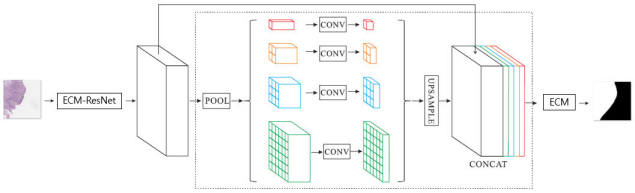

FIGURE 16. The ECM-equipped PSPNet used in the experiment [18]. PSPNet handles multiple scale information with the pyramid pooling module. In the experiment, we modify this PSPNet by replacing the backbone before the pyramid pooling module with the ECM-ResNet and the last convolution layer with the ECM.

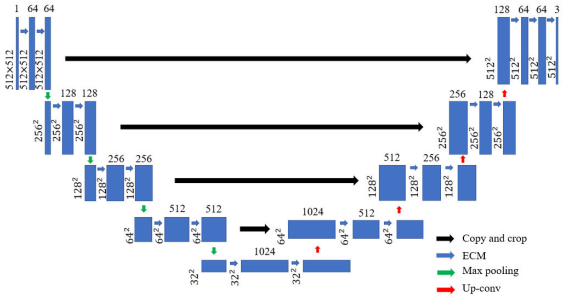

FIGURE 17. The ECM-equipped U-Net used in the experiment [22]. U-Net consists of a contracting path (left-half) to capture context and a symmetric expanding path (right-half) that enables precise localization. In the experiment, convolutions in the contracting and expanding path are replaced by the ECM.

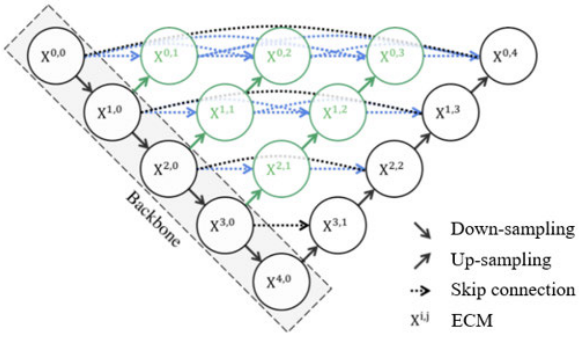

FIGURE 18. The ECM-equipped UNet++ used in the experiment [23]. UNet++ has re-designed skip pathways of U-Net aiming at reducing the semantic gap. The skip pathways convey the features by utilizing convolutions. In the experiment, as well as convolutions in contracting and expanding path, convolutions in skip pathways are also replaced by the ECM.

However, there are still things to improve in our model. The ECM still needs hyperparameter k set by a user, and the intermediate convolutional phase is fixed (convolutions that bring out $1/3 * m$, $2/3 * m$ channels). But despite the inconvenience of hyperparameter setting and such an intuitive module design, the ECM has shown meaningful results. Thus, further studies based on the proposed ECM have room for more performance improvement.

VI. ACKNOWLEDGMENT

De-identified pathology images and annotations used in this research were prepared and provided by the Seoul National University Hospital.

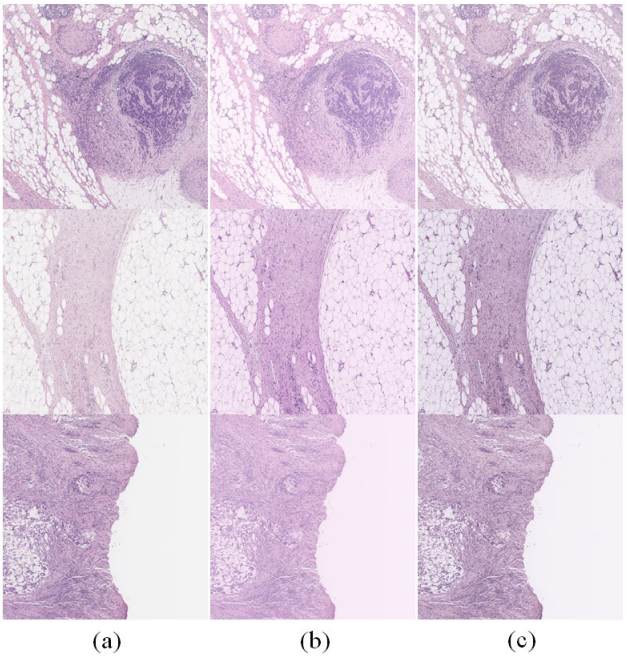

FIGURE 19. Stain normalized images for other methods. (a) H&E stained images (b) stain normalized images applying the method of [43] (c) stain normalized images applying the method of [44].

APPENDIX

See Figures 16–19.

REFERENCES

[1] I. J. Simpson, M. W. Woolrich, M. J. Cardoso, D. M. Cash, M. Modat, J. A. Schnabel, and S. Ourselin, "A Bayesian approach for spatially adaptive regularisation in non-rigid registration," in *Proc. Int. Conf. Med. Image Comput.-Assisted Intervent.* Springer, 2013, pp. 10–18.

[2] F. Yokota, T. Okada, M. Takao, N. Sugano, Y. Tada, N. Tomiyama, and Y. Sato, "Automated ct segmentation of diseased hip using hierarchical and conditional statistical shape models," in *Proc. Int. Conf. Med. Image Comput.-Assisted Intervent.* Springer, 2013, pp. 190–197.

[3] S. Nouranian, S. S. Mahdavi, I. Spadinger, W. J. Morris, S. E. Salcudean, and P. Abolmaesumi, "An automatic multi-atlas segmentation of the prostate in transrectal ultrasound images using pairwise atlas shape similarity," in *Proc. Int. Conf. Med. Image Comput.-Assisted Intervent.* Springer, 2013, pp. 173–180.

[4] H. Eavani, T. D. Satterthwaite, R. E. Gur, R. C. Gur, and C. Davatzikos, "Discriminative sparse connectivity patterns for classification of fmri data," in *Proc. Int. Conf. Med. Image Comput.-Assisted Intervent.* Springer, 2014, pp. 193–200.

[5] R. V. Hartley, "Transmission of information 1," *Bell Syst. Tech. J.*, vol. 7, no. 3, pp. 535–563, 1928.

[6] C. E. Shannon, "A mathematical theory of communication," *ACM SIGMOBILE mobile Comput. Commun. Rev.*, vol. 5, no. 1, pp. 3–55, 2001.

[7] S.-H. Han, J.-H. Lee, and K.-Y. Yu, "An approach for segmentation of airborne laser point clouds utilizing scan-line characteristics," *ETRI J.*, vol. 29, no. 5, pp. 641–648, Oct. 2007.

[8] J. Long, E. Shelhamer, and T. Darrell, "Fully convolutional networks for semantic segmentation," in *Proc. IEEE Conf. Comput. Vis. Pattern Recognit.*, Jun. 2015, pp. 3431–3440.

[9] K. Simonyan and A. Zisserman, "Very deep convolutional networks for large-scale image recognition," 2014, *arXiv:1409.1556*. [Online]. Available: https://arxiv.org/abs/1409.1556

[10] C. Szegedy, W. Liu, Y. Jia, P. Sermanet, S. Reed, D. Anguelov, D. Erhan, V. Vanhoucke, and A. Rabinovich, "Going deeper with convolutions," in *Proc. IEEE Conf. Comput. Vis. Pattern Recognit. (CVPR)*, Jun. 2015, pp. 1–9.

[11] H. Noh, S. Hong, and B. Han, "Learning deconvolution network for semantic segmentation," in *Proc. IEEE Int. Conf. Comput. Vis. (ICCV)*, Dec. 2015, pp. 1520–1528.

[12] V. Badrinarayanan, A. Kendall, and R. Cipolla, "SegNet: A deep convolutional encoder-decoder architecture for image segmentation," *IEEE Trans. Pattern Anal. Mach. Intell.*, vol. 39, no. 12, pp. 2481–2495, Dec. 2017.

[13] J. Wang, K. Sun, T. Cheng, B. Jiang, C. Deng, Y. Zhao, D. Liu, Y. Mu, M. Tan, X. Wang, W. Liu, and B. Xiao, "Deep high-resolution representation learning for visual recognition," *IEEE Trans. Pattern Anal. Mach. Intell.*, early access, Apr. 1, 2020, doi: 10.1109/TPAMI.2020.2983686.

[14] L.-C. Chen, G. Papandreou, I. Kokkinos, K. Murphy, and A. L. Yuille, "Semantic image segmentation with deep convolutional nets and fully connected CRFs," 2014, *arXiv:1412.7062*. [Online]. Available: https://arxiv.org/abs/1412.7062

[15] L.-C. Chen, G. Papandreou, I. Kokkinos, K. Murphy, and A. L. Yuille, "DeepLab: Semantic image segmentation with deep convolutional nets, atrous convolution, and fully connected CRFs," *IEEE Trans. Pattern Anal. Mach. Intell.*, vol. 40, no. 4, pp. 834–848, Apr. 2018.

[16] K. He, X. Zhang, S. Ren, and J. Sun, "Spatial pyramid pooling in deep convolutional networks for visual recognition," *IEEE Trans. Pattern Anal. Mach. Intell.*, vol. 37, no. 9, pp. 1904–1916, Sep. 2015.

[17] L.-C. Chen, G. Papandreou, F. Schroff, and H. Adam, "Rethinking atrous convolution for semantic image segmentation," 2017, *arXiv:1706.05587*. [Online]. Available: https://arxiv.org/abs/1706.05587

[18] H. Zhao, J. Shi, X. Qi, X. Wang, and J. Jia, "Pyramid scene parsing network," in *Proc. IEEE Conf. Comput. Vis. pattern Recognit.*, Jul. 2017, pp. 2881–2890.

[19] L.-C. Chen, Y. Zhu, G. Papandreou, F. Schroff, and H. Adam, "Encoder-decoder with atrous separable convolution for semantic image segmentation," in *Proc. Eur. Conf. Comput. Vis. (ECCV)*, Sep. 2018, pp. 801–818.

[20] C. Li, H. Chen, X. Li, N. Xu, Z. Hu, D. Xue, S. Qi, H. Ma, L. Zhang, and H. Sun, "A review for cervical histopathology image analysis using machine vision approaches," *Artif. Intell. Rev.*, vol. 53, no. 7, pp. 4821–4862, Oct. 2020.

[21] X. Zhou, C. Li, M. M. Rahaman, Y. Yao, S. Ai, C. Sun, Q. Wang, Y. Zhang, M. Li, X. Li, T. Jiang, D. Xue, S. Qi, and Y. Teng, "A comprehensive review for breast histopathology image analysis using classical and deep neural networks," *IEEE Access*, vol. 8, pp. 90931–90956, 2020.

[22] O. Ronneberger, P. Fischer, and T. Brox, "U-Net: Convolutional networks for biomedical image segmentation," in *Proc. Int. Conf. Med. Image Comput.-Assisted Intervent.* Springer, 2015, pp. 234–241.

[23] Z. Zhou, M. M. R. Siddiquee, N. Tajbakhsh, and J. Liang, "UNet++: A nested U-Net architecture for medical image segmentation," in *Deep Learning in Medical Image Analysis and Multimodal Learning Clinical Decision Support*. Springer, 2018, pp. 3–11.

[24] B. Wang, S. Qiu, and H. He, "Dual encoding U-Net for retinal vessel segmentation," in *Proc. Int. Conf. Med. Image Comput.-Assisted Intervent.* Springer, 2019, pp. 84–92.

[25] R. J. Araújo, J. S. Cardoso, and H. P. Oliveira, "A deep learning design for improving topology coherence in blood vessel segmentation," in *Proc. Int. Conf. Med. Image Comput.-Assisted Intervent.* Springer, 2019, pp. 93–101.

[26] D. P Kingma and M. Welling, "Auto-encoding variational bayes," 2013, *arXiv:1312.6114*. [Online]. Available: https://arxiv.org/abs/1312.6114

[27] P. Yin, Q. Wu, Y. Xu, H. Min, M. Yang, Y. Zhang, and M. Tan, "PM-Net: Pyramid multi-label network for joint optic disc and cup segmentation," in *Proc. Int. Conf. Med. Image Comput.-Assisted Intervent.* Springer, 2019, pp. 129–137.

[28] K. He, G. Gkioxari, P. Dollár, and R. Girshick, "Mask R-CNN," in *Proc. IEEE Int. Conf. Comput. Vis.*, Oct. 2017, pp. 2961–2969.

[29] Y. Wu, Y. Xia, Y. Song, D. Zhang, D. Liu, C. Zhang, and W. Cai, "Vessel-Net: Retinal vessel segmentation under multi-path supervision," in *Proc. Int. Conf. Med. Image Comput.-Assisted Intervent.* Springer, 2019, pp. 264–272.

[30] K. Qi, H. Yang, C. Li, Z. Liu, M. Wang, Q. Liu, and S. Wang, "X-Net: Brain stroke lesion segmentation based on depthwise separable convolution and long-range dependencies," in *Proc. Int. Conf. Med. Image Comput.-Assisted Intervent.* Springer, 2019, pp. 247–255.

[31] Y. Liu, J. Li, Y. Wang, M. Wang, X. Li, Z. Jiao, J. Yang, and X. Gao, "Refined segmentation R-CNN: A two-stage convolutional neural network for punctate white matter lesion segmentation in preterm infants," in *Proc. Int. Conf. Med. Image Comput.-Assisted Intervent.* Springer, 2019, pp. 193–201.

[32] C. Li, H. Chen, L. Zhang, N. Xu, D. Xue, Z. Hu, H. Ma, and H. Sun, "Cervical histopathology image classification using multilayer hidden conditional random fields and weakly supervised learning," *IEEE Access*, vol. 7, pp. 90378–90397, 2019.

[33] C. Sun, C. Li, J. Zhang, M. M. Rahaman, S. Ai, H. Chen, F. Kulwa, Y. Li, X. Li, and T. Jiang, "Gastric histopathology image segmentation using a hierarchical conditional random field," *Biocybern. Biomed. Eng.*, vol. 40, no. 4, pp. 1535–1555, Oct. 2020.

[34] C. Li, Z. Hu, H. Chen, S. Ai, J. Zhang, Y. Zhang, Q. Wang, and X. Li, "A cervical histopathology image clustering approach using graph based features," *Social Netw. Comput. Sci.*, vol. 2, no. 2, pp. 1–20, Apr. 2021.

[35] J. Xu, X. Luo, G. Wang, H. Gilmore, and A. Madabhushi, "A deep convolutional neural network for segmenting and classifying epithelial and stromal regions in histopathological images," *Neurocomputing*, vol. 191, pp. 214–223, May 2016.

[36] D. Xue, X. Zhou, C. Li, Y. Yao, M. M. Rahaman, J. Zhang, H. Chen, J. Zhang, S. Qi, and H. Sun, "An application of transfer learning and ensemble learning techniques for cervical histopathology image classification," *IEEE Access*, vol. 8, pp. 104603–104618, 2020.

[37] J. Xu, H. Lu, H. Li, C. Yan, X. Wang, M. Zang, D. G. D. Rooij, A. Madabhushi, and E. Y. Xu, "Computerized spermatogenesis staging (CSS) of mouse testis sections via quantitative histomorphological analysis," *Med. Image Anal.*, vol. 70, May 2021, Art. no. 101835.

[38] S. Woo, J. Park, J.-Y. Lee, and I. S. Kweon, "CBAM: Convolutional block attention module," in *Proc. Eur. Conf. Comput. Vis. (ECCV)*, Sep. 2018, pp. 3–19.

[39] K. He, X. Zhang, S. Ren, and J. Sun, "Deep residual learning for image recognition," in *Proc. IEEE Conf. Comput. Vis. Pattern Recognit.*, Jun. 2016, pp. 770–778.

[40] D. P. Kingma and J. Ba, "Adam: A method for stochastic optimization," 2014, *arXiv:1412.6980*. [Online]. Available: https://arxiv.org/abs/1412.6980

[41] K. He, X. Zhang, S. Ren, and J. Sun, "Delving deep into rectifiers: Surpassing human-level performance on imagenet classification," in *Proc. IEEE Int. Conf. Comput. Vis.*, Dec. 2015, pp. 1026–1034.

[42] M. Macenko, M. Niethammer, J. S. Marron, D. Borland, J. T. Woosley, X. Guan, C. Schmitt, and N. E. Thomas, "A method for normalizing histology slides for quantitative analysis," in *Proc. IEEE Int. Symp. Biomed. Imag., From Nano Macro*, Jul. 2009, pp. 1107–1110.

[43] E. Reinhard, M. Adhikhmin, B. Gooch, and P. Shirley, "Color transfer between images," *IEEE Comput. Graph. Appl.*, vol. 21, no. 4, pp. 34–41, Jul. 2001.

[44] A. Vahadane, T. Peng, A. Sethi, S. Albarqouni, L. Wang, M. Baust, K. Steiger, A. M. Schlitter, I. Esposito, and N. Navab, "Structure-preserving color normalization and sparse stain separation for histological images," *IEEE Trans. Med. Imag.*, vol. 35, no. 8, pp. 1962–1971, Aug. 2016.

[45] K. Clark, B. Vendt, K. Smith, J. Freymann, J. Kirby, P. Koppel, S. Moore, S. Phillips, D. Maffitt, M. Pringle, L. Tarbox, and F. Prior, "The cancer imaging archive (TCIA): Maintaining and operating a public information repository," *J. Digit. Imag.*, vol. 26, no. 6, pp. 1045–1057, Dec. 2013.

HWA-RANG KIM received the B.S. and M.S. degrees in electronics engineering from Kyungpook National University (KNU), Daegu, South Korea, in 2018 and 2020, respectively, where he is currently pursuing the Ph.D. degree with the Graduate School of Electronic and Electrical Engineering. His research interests include computer vision and pattern recognition.

KWANG-JU KIM (Associate Member, IEEE) received the B.S. degree in electronics engineering from Kyungpook National University (KNU), Daegu, South Korea, in 2010, and the M.S. degree in electrical engineering from the Pohang Institute of Science and Technology (POSTECH), Pohang, South Korea, in 2013. From 2013 to 2015, he was a Researcher with General Electric. Since 2015, he has been with the Electronics and Telecommunications Research Institute, Daejeon, Republic of Korea. His major research interests include computer vision, pattern recognition, and video surveillance.

KIL-TAEK LIM received the B.S., M.S., and Ph.D. degrees in electronics engineering from the Department of Electronics Engineering, Kyungpook National University, Daegu, Republic of Korea, in 1993, 1995, and 1999, respectively. From 2004 to 2011, he was an Assistant Professor with the Computer and Information Engineering Department, Gyeongju University, Republic of Korea. Since 2012, he has been with the Electronics and Telecommunications Research Institute, Daejeon, Republic of Korea. His major research interests include computer vision, pattern recognition, and video surveillance.

DOO-HYUN CHOI received the B.S. degree in electronics engineering from Kyungpook National University (KNU), Daegu, South Korea, in 1991, and the M.S. and Ph.D. degrees in computer science and engineering from the Pohang Institute of Science and Technology (POSTECH), Pohang, South Korea, in 1993 and 1996, respectively. He served as an Assistant Professor with KNU, from 1996 to 2000, and Seoul National University, from 2000 to 2003. In 2003, he rejoined at KNU and became a Full Professor with the School of Electronics Engineering. He currently serves as the Head for the Department of Mobile Engineering supported by Samsung Electronics and an in charge for the Intelligent Information Systems Laboratory, KNU. His research/educational interests include intelligent information and signal processing systems and practical development capacity building of future generations.